Check for updates

Cofactor-free oxidase-mimetic nanomaterials from self-assembled histidine-rich peptides

Qing Liu[1,5], Kaiwei Wan [1,5], Yingxu Shang[1], Zhen-Gang Wang[2✉], Yiyang Zhang[3], Luru Dai[1], Chen Wang [1,4], Hui Wang[1✉], Xinghua Shi [1,4], Dongsheng Liu[3] and Baoquan Ding [1,4✉]

Natural oxidases mainly rely on cofactors and well-arranged amino acid residues for catalysing electron-transfer reactions but suffer from non-recovery of their activity upon externally induced protein unfolding. However, it remains unknown whether residues at the active site can catalyse similar reactions in the absence of the cofactor. Here, we describe a series of self-assembling, histidine-rich peptides, as short as a dipeptide, with catalytic function similar to that of haem-dependent peroxidases. The histidine residues of the peptide chains form periodic arrays that are able to catalyse H_2O_2 reduction reactions efficiently through the formation of reactive ternary complex intermediates. The supramolecular catalyst exhibiting the highest activity could be switched between inactive and active states without loss of activity for ten cycles of heating/cooling or acidification/neutralization treatments, demonstrating the reversible assembly/disassembly of the active residues. These findings may aid the design of advanced biomimetic catalytic materials and provide a model for primitive cofactor-free enzymes.

A considerable number of redox enzymes catalyse chemical transformations with the assistance of cofactors. The unfolding of proteins, caused by acidification or heating, can induce irreversible inactivation of the enzymes due to the disordering of the essential residues and the dislocation of cofactors. Several oxygenases and oxidases do not require cofactors for catalysis; instead, neighbouring residues at the active site participate in the catalysis[1–3]. However, once unfolded, it is difficult for the dissociated residues to reorganize to form the active sites upon renaturation of proteins.

Enzyme-inspired supramolecular catalysts[4–8] hold promise in cofactor-free catalysis. Such catalysts may lead us to resolve the mechanisms by which simple molecules evolved into cofactor-dependent enzymes, because the hot, acidic primordial soup was unsuitable for the action of proteinaceous enzymes and the multi-step biosynthesis of cofactors[9]. Simple peptides with repeated amino acid sequences exhibit a myriad of conformational variations that allow a spatial grouping of residues amenable to biological activity[10–12], and it has been suggested that they self-assembled into the earliest proteins[13–15]. Indeed, it is possible that the catalytic functions of modern cofactor-containing active sites were first performed by primitive enzymes relying solely on the periodic arrangement of the reactive residues.

Haemoproteins, with a haem as the cofactor, are ubiquitous in nature. In peroxidases, myoglobin, haemoglobin or artificial haem complexes, haem is cooperatively assisted by a proximal and a distal histidine to catalyse electron-transfer reactions[16–19]. It is thus hypothesized that histidine residues may have contributed to the reactions catalysed by primitive haemoprotein analogues that did not contain haem. Indeed, metal-free histidine-containing pairs or triads in supramolecular self-assemblies have exhibited enzyme-like

hydrolytic activities[10,20–22]. However, cofactor-free, histidine-catalysed redox reactions have not yet been reported. Histidine's imidazole nitrogens can participate in hydrogen-bonding interactions as acceptors or donors[23]. Moreover, histidine-rich peptides have shown the ability to form β-sheets[19]. This may allow an orientation of the side-chain imidazole in such a way to synergistically activate H_2O_2 reduction reactions.

Metal-free catalysts, such as heteroatom-doped carbon nanomaterials (for example, graphene or carbon nitride)[24–27], conducting polymers[28] or supramolecular systems[29,30], are of interest for their ability to catalyse H_2O_2/O_2 reduction reactions. A feature key to the activities of these catalysts is their π-conjugation, which is ascribed to the charge redistribution[26] or charge transport effect[29]. By contrast, here, we report a cofactor-free, non-conjugated supramolecular catalyst exhibiting redox activity that is dependent on the cooperation between neighbouring functional groups. We assembled oligohistidine peptides, containing NH_3^+ and COO^- terminal groups, into ordered nanostructures with a crystal-like lattice that exhibit activity in H_2O_2 reduction and disproportionation (Fig. 1). The activity of the catalysts can be recovered after ten or more cycles of thermal or acid treatment, making them more robust than haemin-containing complexes.

Structures of the peptide self-assemblies
To gain insight into the structures of the supramolecular assemblies, we examined the concentration-dependent circular dichroism (CD) signals and absorbances of oligomeric histidine peptides, ranging from monomeric histidine (that is, H1) to a 20-residue peptide (that is, H20; Supplementary Fig. 1a,b). The peptides ranging from H2 to H20 all adopted a β-sheet conformation, whereas H1 showed no signals arising from β-sheet formation. H15 showed the strongest
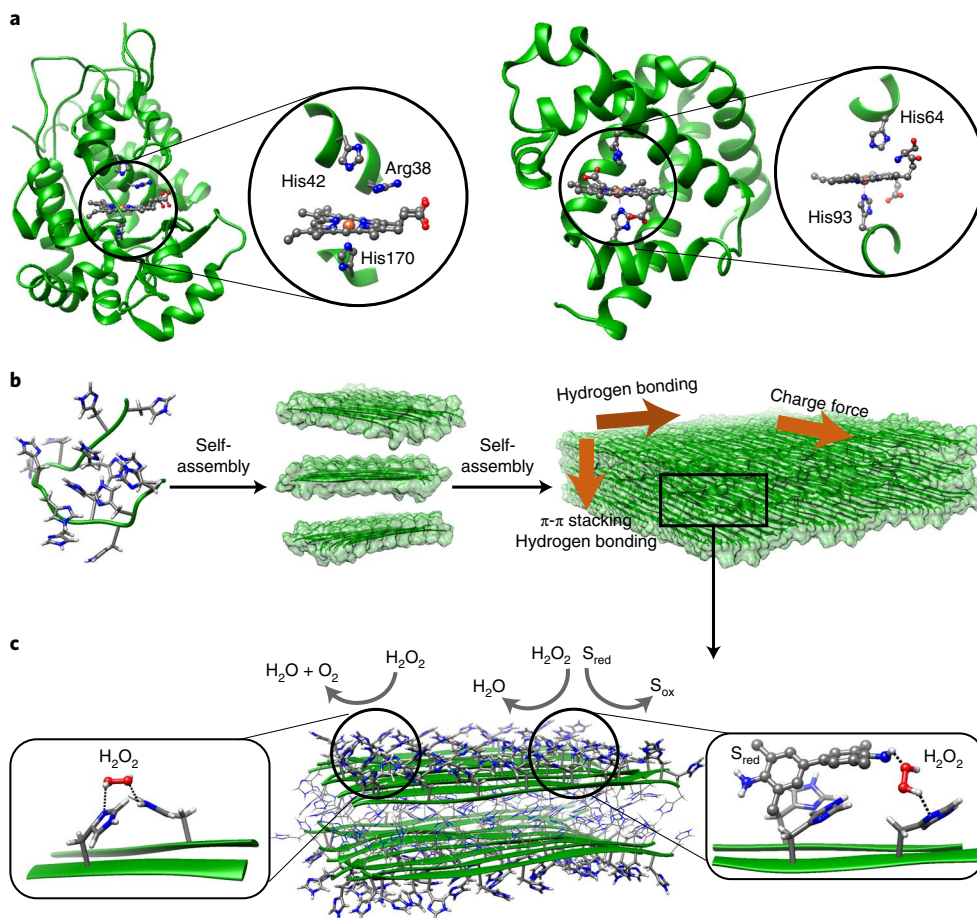
Fig. 1 | Design of haem-free self-assembling oligohistidine catalysts inspired by natural haem-containing enzymes. a, Structures of horseradish peroxidase (left) and sperm whale myoglobin (right) showing the haem cofactor and catalytic residues distributed in the active sites. **b**, Schematic illustration showing the self-assembly of the designed peptides into β-sheets and planar crystal nanomaterials through charge interactions, hydrogen bonding and π–π stacking. **c**, Working model of the periodically arranged peptide chains and side-chain groups for catalysing H_2O_2 reduction and disproportionation reactions. The insets show schematic illustrations of the binding of the catalysts to the substrates to form reactive intermediates. The peptides are rich in histidine residues to afford a high density of active sites on the catalyst surfaces. No other residues are involved so that the catalytic mechanism can be elucidated. NH_3^+ and COO^- terminals would favour the connection of the chains through electrostatic interactions.

CD intensity among all the oligohistidine peptides. Supplementary Fig. 1c shows the plots of CD intensity normalized to the histidine concentration, shown as the molar residue ellipticity (MRE), against the peptide concentration. As the peptide concentration increased, the MRE values increased, and then unexpectedly decreased. The enhancement can be ascribed to enhanced concentration-induced peptide self-assembly. Additionally, a redshift in absorbance was observed as the peptide concentration increased (Supplementary Fig. 2), indicating enhanced interchain (for example, π-stacking[31,32]) interactions. It is inferred that the decrease in MRE at higher peptide concentrations may be caused by the increased sizes of the nanostructures, which affects the light scattering[33]. To investigate the peptide length dependence of β-sheet formation, we plotted the CD intensity (Fig. 2a and Supplementary Fig. 3), maximum absorbance wavelength (Fig. 2a) and full-width at half-maxima (FWHM; Supplementary Fig. 4) against the peptide length. The results indicate the cooperation of the residues in facilitating β-sheet formation. The critical β-sheet-forming concentration (CβC), at which the β-sheet CD signals emerged, was also plotted against the peptide length (Fig. 2b and Supplementary Fig. 5). The data confirm a stronger self-assembly propensity for longer peptides.

Fourier transform infrared (FTIR) spectroscopy revealed parallel β-sheet structures for H2 to H20 at different concentrations

(Supplementary Fig. 6), as indicated by the spectral feature in the amide I region (a typical component at ~1,630 cm^{-1} and no component at ~1,695 cm^{-1})[34,35]. When the peptide concentration was lower than the CβC, no signals corresponding to β-sheets were found. Scanning electron microscopy (SEM) images (Fig. 2c and Supplementary Figs. 7–10), scanning transmission electron microscopy (STEM) imaging and elemental mapping (Supplementary Fig. 11), and optical microscopy images (Fig. 2d, Supplementary Fig. 12 and Supplementary Videos 1–4) revealed that the peptides with lengths ranging from 2 to 15 residues formed large two-dimensional nanosheets or ribbons, and that the sizes reached up to millimetres. The peptides with 16 and 20 residues showed granular morphologies (Supplementary Figs. 13 and 14).

Powder X-ray diffraction (XRD) analysis showed similar patterns for the H2, H5, H7, H10, H12 and H15 peptides (Supplementary Fig. 15). The typical selective-area electron diffraction (SAED) pattern recorded perpendicularly to the surfaces revealed a good single-crystalline nature of the strongest β-sheet forming H15 nanostructures (Fig. 3a and Supplementary Fig. 16), which was corroborated by high-resolution transmission electron microscopy (HRTEM) imaging (Fig. 3b and Supplementary Fig. 17). The SAED patterns and HRTEM images of the H2-assembled nanosheets are shown in Supplementary Figs. 18 and 19. By contrast, neither SAED
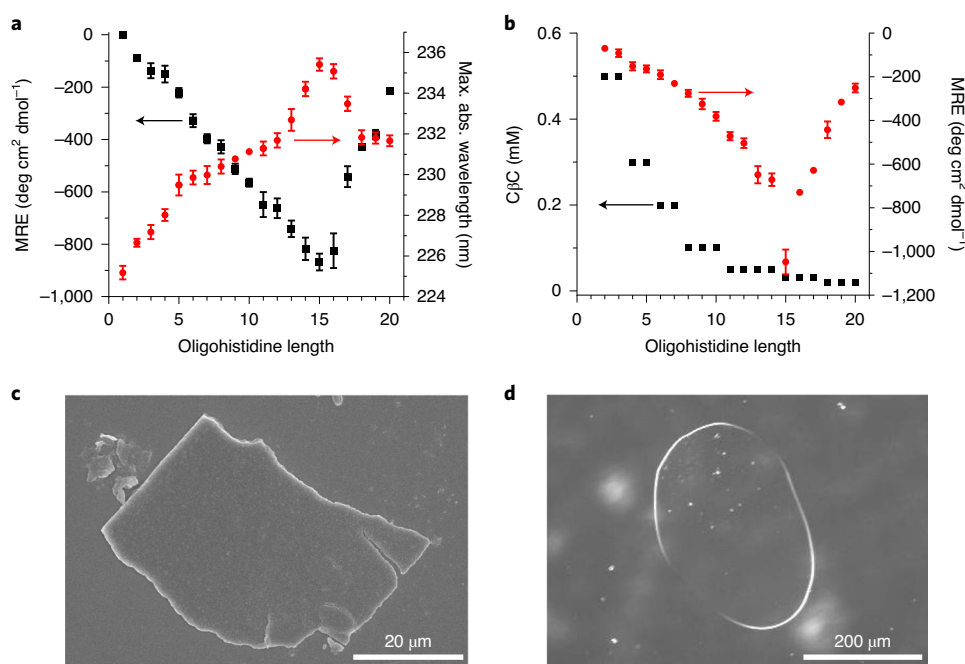
Fig. 2 | Structural characterization of the peptide-assembled catalysts. a, Effect of peptide length on CD intensity and maximum absorbance wavelength (1 mM peptide). From H1 to H15, a linear increase is observed for the normalized CD intensity. From H15 to H20, a decrease in CD intensity is observed. Consistent with these observations, a redshift in the absorbance and an increase in FWHM are observed for H1 to H15, and a blueshift and a decrease in FWHM are observed from H15 to H20. **b**, The CβC values and the corresponding CD intensities at the indicated peptide lengths. The CβC value decreased as the peptide length increased, with H15 exhibiting the highest MRE at its CβC. The data in **a** and **b** are presented as the mean ± s.d., with the error bars representing the s.d. and $N = 3$. **c,d**, SEM image (**c**) and optical microscopy image (**d**) of the nanostructures assembled from the H15 peptide.

patterns nor lattice fringes were observed for H16 and H20, and their XRD patterns were remarkably distinct from those of H2–H15 (Supplementary Fig. 15), which is congruent with the amorphous structures of H16 and H20.

Structural modelling

We performed a first-principles calculation to elucidate the molecular packing of the H15 molecules in the crystals. The simulation of the single crystal (Crystallographic Data 2) revealed that H15 molecules form a triclinic unit cell (Fig. 3c) with the $R1$ space group and unit cell parameters $a = 101.853(0)$ Å, $b = 4.445(3)$ Å, $c = 9.201(6)$ Å and $\alpha = 85.1705°$, $\beta = 90.3193°$, $\gamma = 88.9551°$. The diffraction peaks in the XRD pattern simulated using this single-crystal data matched those of the powder XRD pattern obtained from the bulk single crystal (Supplementary Fig. 20). The d spacing of 0.486 nm, estimated from the SAED pattern, corresponds to the interlattice spacing of the (010) planes of the H15 crystal, whereas lattice fringes with a spacing of 0.48 nm, attributed to the average distance between the α-carbons of the β-strands, were evident in the HRTEM image (Fig. 3d). The d spacing of 8.86 Å, estimated from the SAED pattern, corresponds to the interlattice spacing of the (001) planes of the H15 crystal. Other typical planes revealed by the SAED pattern and HRTEM image are shown in Supplementary Fig. 21. By replacing the COOH with acetyl, we observed an enhanced β-sheet CD response, but an amorphous structure under TEM (Supplementary Fig. 22). These results validate the importance of the electrostatic interactions in the formation of the crystal structures, and implies that the β-sheet was not the only factor for the periodic self-assembly. We also performed a simulation of H2 self-assembly. We found that β-strands of the H2 peptide were synergistically stabilized by interstrand hydrogen bonding, π–π stacking and electrostatic interactions (Supplementary Fig. 23), which indicates a less efficient β-sheet formation of H2 (Fig. 2a,b).

Critical lengths of peptides

When the peptide length was two residues or more, the peptide self-assembled with extended conformations, resulting in well-ordered chain arrangements. The cooperation between residues in stabilizing the β-sheets was stronger in longer peptides, because intermolecular hydrogen bonding was sufficiently strong to form β-sheets from the long peptides. It is also noteworthy that the redshift in the absorbance (Fig. 2c) and increase in FWHM (Supplementary Fig. 5) occurring from H12 to H15 were enhanced. The side-chain group, imidazole, is hydrophilic (hydrophobicity scale, −3.2). Thus, the periodicity of the chain self-assembly may also be affected by water molecules, which would be more pronounced for shorter peptides. The peptides with more than 12 residues had further enhanced interchain interactions along three directions, protecting against water interference and facilitating the formation of ordered structures. On the other hand, long peptides may also have a greater chance of chain entanglement, which may account for the disordered structures of H16 and H20. We conclude that H2, H12 and H15 are the peptides of critical length.

Quantitative structure–activity relationship

We investigated the catalytic activity of H15 with 3,3′,5,5′-tetramethylbenzidine (TMB) and H_2O_2 as substrates. An increase in the spectrophotometric absorbance at 652 nm was observed, which was attributed to a one-electron oxidation of TMB into its charge-transfer complex by H_2O_2 (Supplementary Fig. 24a). However, no further oxidation of TMB into the diimine, which has a maximum absorbance at 450 nm (ref. [36]), was observed. The H15 catalyst also showed activity in the oxidation of chromogenic NADH to NAD⁺ by H_2O_2 (Supplementary Fig. 24b), and of homovanillic acid (HVA) to the fluorescent 2,2′-dlhydroxy-3,3′-dimethoxybiphenyl-5,5′-diacetic acid (HVA dimer) also by H_2O_2 (Supplementary Fig. 24c). These results indicate that the peptides
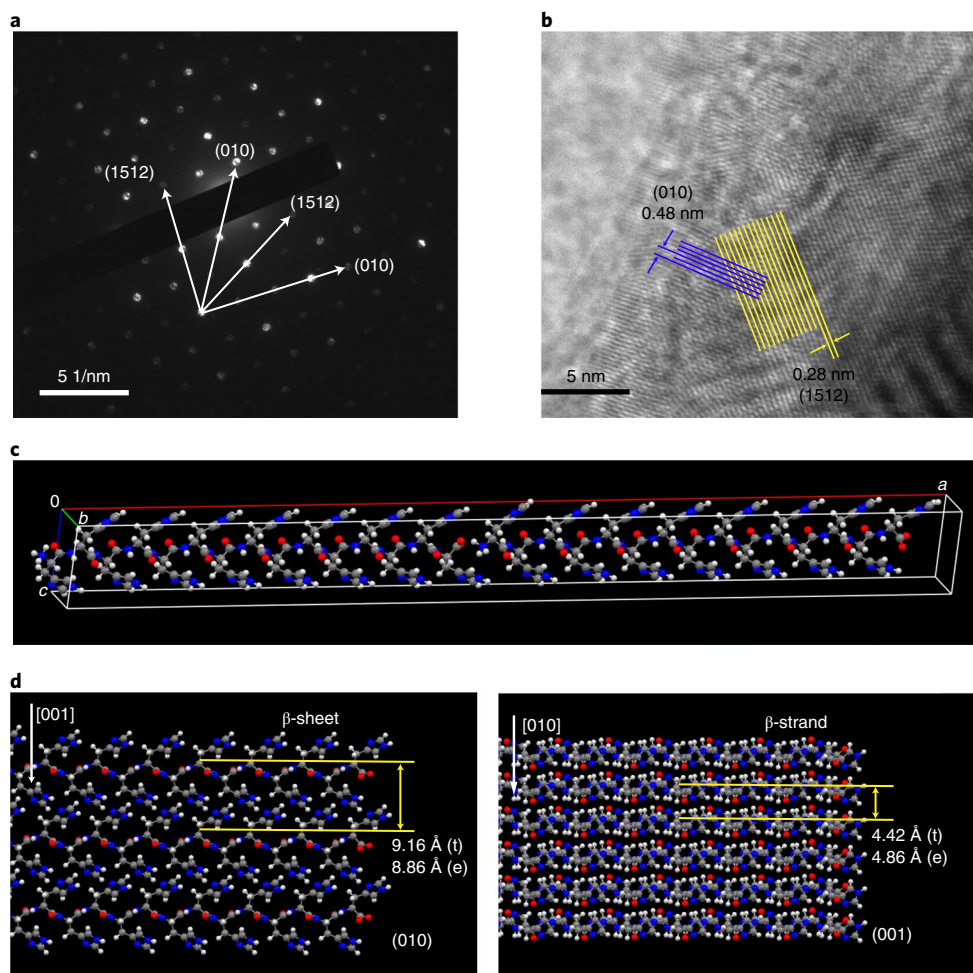
Fig. 3 | Crystal lattice of the peptide nanostructures and peptide chain arrangement patterns. a,b, SAED pattern (**a**) and HRTEM image (**b**) of the H15-based nanostructures (1 mM peptide). **c**, A theoretical model of the molecular packing in the orthogonal unit cell of the H15 crystal. Each unit contains two H15 molecules linked through electrostatic interactions. **d**, The packing of neighbouring β-sheets on the (010) facet along the [001] direction (left) and the neighbouring β-strands on the (001) facet along the [010] direction (right). The theoretical (t) and experimental (e) spacing between β-sheets or between β-strands are indicated. The facets marked on the SAED pattern and HRTEM image were estimated on the basis of a simulation. N, O, C and H atoms are indicated in blue, red, dark grey and light grey, respectively. The peptides effectively formed a large structure through interstrand hydrogen bonding along the β-sheet, electrostatic interactions between the NH_3^+ and COO^- terminals along the β-strands and π–π stacking of the side chains perpendicular to the β-sheet. A periodic arrangement of the main- and side-chain groups was formed.

show horseradish peroxidase-mimicking activity. No catalytic oxidation of these substrates was observed for H1 up to 10 mM.

We varied the number of histidine (His) residues and peptide concentration to investigate their catalytic activity. With TMB as the reducing substrate, the activities of the peptides (the initial catalytic velocity, V_i) reached saturation at different concentrations (Supplementary Figs. 25–27). The activities normalized to the concentration of peptide chains, that is, the value of V_i (per mM peptide), were plotted against peptide concentration (Fig. 4a and Supplementary Fig. 28). The value of V_i (per mM peptide) was enhanced for a certain range of peptide concentration. According to the CD and maximum absorbance shift data (Fig. 2a,b and Supplementary Fig. 5), it can be concluded that higher peptide concentrations may facilitate the formation of larger amounts of active sites by promoting the ordered self-assembly of the peptides. To evaluate the peptide length-dependence of activity, the activities normalized to the residue concentration (V_i (per mM His)) were plotted against peptide length at different peptide concentrations (Fig. 4b and Supplementary Fig. 29). A value for V_i (per mM His) emerged only when the number of residues reached 2, remained

almost unchanged from H2 to H12, grew exponentially from H12 to H15 and decreased rapidly for peptides with over 16 residues. The V_i (per mM His) values reflect the cooperation between the residues. This tendency is consistent with the length-dependent signals of molecular conformation (β-sheet) and crystal structures, which identified H2, H12 and H15 as the peptides of critical length. It also indicates that the activity does not solely rely on the β-sheet, but on the formation of crystal structures with β-sheets as building blocks. As presented in Supplementary Fig. 30, the acetylated peptides that showed markedly stronger β-sheet CD signals but formed amorphous structures exhibited much lower activity than the peptides with NH_3^+ and COO^- terminals, confirming the key feature of crystal nanostructure formation in the catalysis. Similar dependencies of V_i (per mM peptide) on peptide concentration and length in the oxidation of both NADH (Supplementary Figs. 31–33) and HVA (Supplementary Figs. 34–36) were also observed.

Kinetics of catalytic activity

To investigate the enzyme kinetics, we plotted V_i against the concentration of the substrate TMB or H_2O_2 in the presence
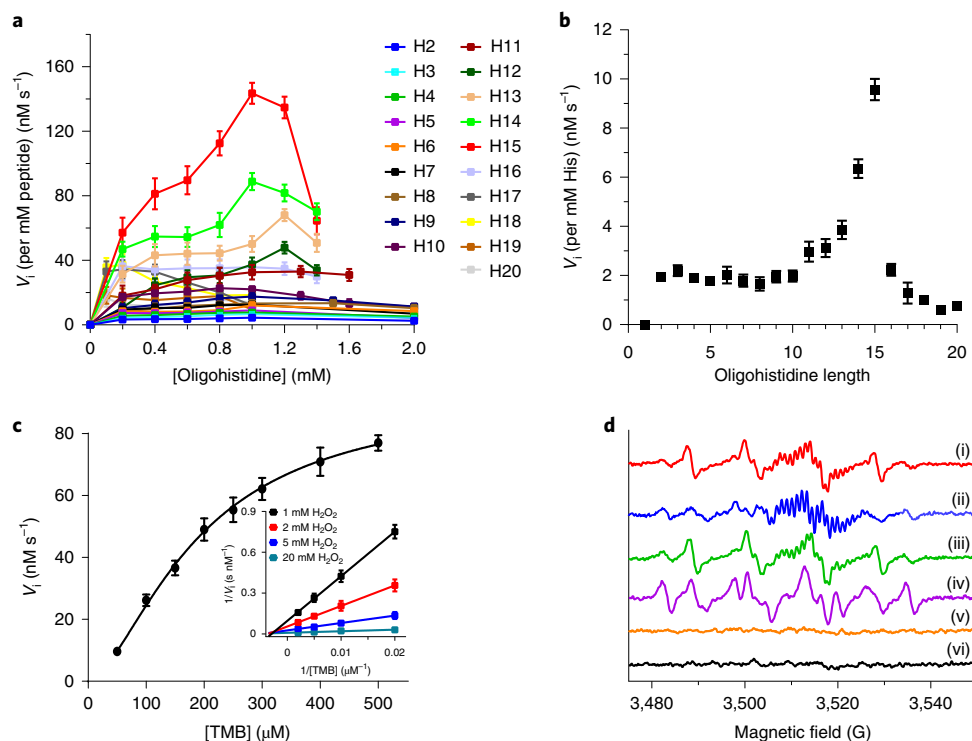
Fig. 4 | Functional characterization of the peptide-assembled catalysts. a, Effect of peptide concentration on V_i (per mM peptide) in the oxidation of TMB by H_2O_2 at the indicated peptide lengths. $[H_2O_2] = 20$ mM, $[TMB] = 0.3$ mM. **b**, The effect of peptide length on V_i (per mM histidine residue) at 1 mM peptide. H2, H12 and H15 were observed to be the peptides of critical lengths. $[H_2O_2] = 20$ mM, $[TMB] = 0.3$ mM. **c**, Global fitting of V_i vs TMB concentration plots under saturated H_2O_2 concentration. The inset presents Lineweaver–Burk plots of the oxidation of TMB by H_2O_2 catalysed by H15, showing that it follows a Michaelis–Menten model of enzymatic reactions and a ternary complex mechanism. It is hypothesized that H_2O_2 forms a complex with TMB and histidine residues on the catalyst surface. $[H15] = 700\,\mu M$. The data in **a–c** are presented as the mean ± s.d., with the error bars representing the s.d. and $N = 3$. **d**, EPR spectra of reaction systems containing H15/H_2O_2/TMB/BMPO/DMSO (i), H15/H_2O_2/TMB/SOD/BMPO/DMSO (ii), H15/H_2O_2/TMB/TBA/BMPO/DMSO (iii), H15/H_2O_2/BMPO/DMSO (iv), H15/TMB/BMPO/DMSO (v) and H_2O_2/TMB/BMPO/DMSO (vi). No EPR signals were observed for the mixture of H_2O_2, TMB and DMSO in the absence of H15. $[H15] = 700\,\mu M$, $[H_2O_2] = 1$ mM, $[TMB] = 0.3$ mM, $[SOD] = 100\,\mu M$, $[TBA] = 100$ mM.

of 0.7 mM H15. The global fitting approach (Fig. 4c and Supplementary Fig. 37) was used to evaluate the turnover frequency and catalytic efficiency, which gave values of $k_{cat}^{TMB} = (1.322 \pm 0.050) \times 10^{-4}\,s^{-1}$, $k_{cat}^{TMB}/K_M^{TMB} = (0.704 \pm 0.071)\,M^{-1}\,s^{-1}$ and $k_{cat}^{H_2O_2} = (1.147 \pm 0.045) \times 10^{-4}\,s^{-1}$, $k_{cat}^{H_2O_2}/K_M^{H_2O_2} = (3.13 \pm 0.46) \times 10^{-2}\,M^{-1}\,s^{-1}$ (mean ± s.d., number of replicates, $N = 3$). The turnover number (= moles product/moles catalyst) was calculated to be 0.0164. The Lineweaver–Burk plots of $1/V_i$ against $1/[TMB]$ or $1/[H_2O_2]$ produced a series of straight lines intersecting at a single point to the left of the ordinate (Fig. 4c inset and Supplementary Fig. 38), consistent with the formation of a ternary complex intermediate. Similar catalysis kinetics were also observed for the catalysed oxidation of NADH (Supplementary Fig. 39).

Reactive species involved in the catalysis

To identify the catalytic mechanism, we used electron paramagnetic resonance (EPR) spectroscopy to identify the possible reactive oxygen species (ROS) formed as intermediate during the catalytic process using 5-*tert*-butoxycarbonyl-5-methyl-1-pyrroline *N*-oxide (BMPO) as the spin-trapping reagent. Dimethylsulfoxide (DMSO) was added to stabilize $HO_2^{\bullet}/O_2^{\bullet-}$, and can also react with $OH^{\bullet}$ to yield the $CH_3^{\bullet}$ radical. In the presence of H_2O_2, TMB and H15, the EPR spectra showed a 1:1:1:1 quadruple peak (Fig. 4d), consistent with the pattern of the typical BMPO–$HO_2^{\bullet}/O_2^{\bullet-}$ spin adduct. Simulated EPR spectra are shown in Supplementary Fig. 40. The g

factor and hyperfine coupling constants for the BMPO adducts were as follows: $g = 2.00633$, $a^N = 13.9478\,G$, $a^H = 12.295\,G$, revealing the formation of the BMPO–$HO_2^{\bullet}/O_2^{\bullet-}$ spin adduct. It is noteworthy that an additional radical signature was also generated in the EPR pattern (Fig. 4d), even in the absence of the spin-trapping reagent (Supplementary Fig. 40). We did not observe this in the absence of H_2O_2 or the catalyst (Fig. 4d(v),(vi)). We thus conclude that the hyperfine coupling can be attributed to TMB radical cations (TMB$^{\bullet+}$; see the hyperfine parameters in Supplementary Fig. 40)[37]. The integrated simulated spectrum of the TMB$^{\bullet+}$ and BMPO–$HO_2^{\bullet}/O_2^{\bullet-}$ spin adduct (Fig. 4d(i) and Supplementary Fig. 40) is consistent with the observed EPR spectrum of the H15/H_2O_2/TMB/BMPO sample.

To further identify the ROS species, superoxidase dismutase (SOD), which catalyses the partitioning of $O_2^{\bullet-}/HO_2^{\bullet}$ into O_2 and H_2O_2, and *tert*-butyl alcohol (TBA), which is a well-known $OH^{\bullet}$ radical scavenger, were added to the system. The addition of SOD substantially decreased the catalytic activity of H15 (Supplementary Fig. 41) and the intensity of the EPR peaks (Fig. 4d(ii)), whereas TBA had no such effect (Fig. 4d(iii) and Supplementary Fig. 41). Interestingly, the EPR spectrum of a H15/H_2O_2 solution exhibited the pattern of the BMPO–$CH_3^{\bullet}$ adduct ($g = 2.00627$, $a^N = 15.2067\,G$, $a^H = 21.9741\,G$), arising from the reaction of DMSO with $OH^{\bullet}$ (Fig. 4d(iv) and Supplementary Fig. 42). This indicates that (1) the $O_2^{\bullet-}/HO_2^{\bullet}$ detected in the H15/H_2O_2/TMB system may be involved in the formation of the ternary complex intermediate and (2) the homocleavage of the O–O bonds in H_2O_2 and the catalysed
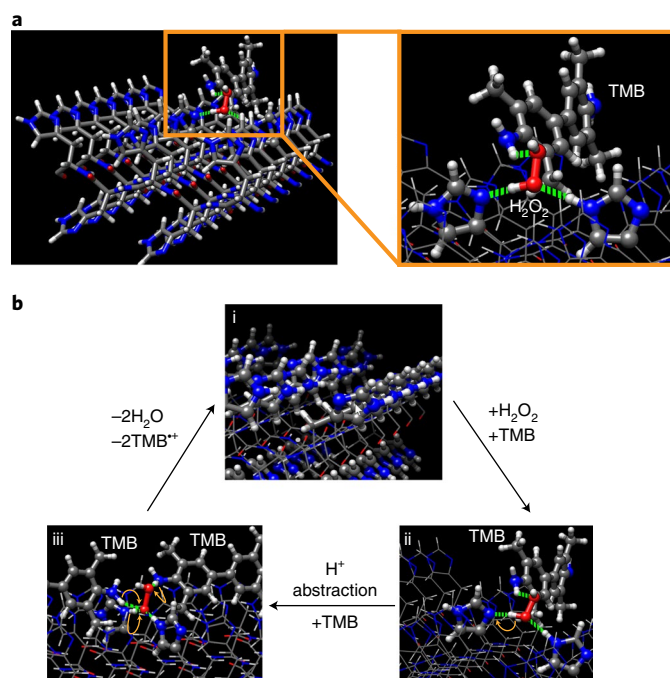
Fig. 5 | Theoretical model of the catalytic process. a, Density functional theory model of the ternary complex intermediate. This model was built on the facet (010), based on the molecular docking of TMB on the catalyst, and optimized by density functional theory. **b**, Proposed transformation process based on the observed signals deriving from OOH• in the EPR spectra (Fig. 4d) and the important roles of OOH• in the catalysis: (i) the resting-state (010) facet, (ii) hydrogen transfer from H_2O_2 to imidazole/generation of superoxide radicals, hydrogen transfer from imidazole–H and TMB to the superoxide radicals, and (iii) the formation and release of H_2O and colourimetric TMB•+ in equilibrium with the charge-transfer complex ($\lambda_{abs} = 652$ nm). N, O, C and H atoms are shown in blue, red, dark grey and light grey, respectively. A large number of repetitively arranged active sites are created by the ordered assembly of the peptides and residues.

decomposition occurred when it adsorbed onto the catalyst (Supplementary Fig. 43), which was notably slowed by TBA (Supplementary Fig. 44). No BMPO–CH₃• adducts were observed in the H15/H_2O_2/TMB system. These results indicate that TMB may have a higher affinity for the catalyst surface, and that the preceding adsorption of TMB is critical to the formation of the ternary complex. This hypothesis was tested by preincubation of the catalyst with H_2O_2 or TMB before mixing with the other substrate (Supplementary Fig. 45 and Discussion 1).

Catalytic mechanism
Based on the catalysis kinetics and EPR results, we performed molecular docking and quantum chemical calculations to simulate the formation of the ternary complex reactive intermediate, which is a key event leading to the subsequent catalytic reactions. The docking results showed that when added to the catalyst alone, H_2O_2 (producing hydroxyl radicals and disproportionation, Supplementary Figs. 43 and 44d) and TMB bind to the β-sheet-based catalyst through non-covalent interactions (Supplementary Fig. 46). When TMB and H_2O_2 were simultaneously added to the catalyst, the adsorption of TMB was energetically favoured, and H_2O_2 could diffuse to the TMB–catalyst complex to form a ternary intermediate through hydrogen bonding and π–π interactions (Fig. 5a). Figure 5b shows the possible pathway for the subsequent transformations. It is hypothesized that the generation of the OOH• species is a result of the transfer of a proton in the ternary complex intermediate from

H_2O_2 to imidazole, with concomitant electron transfer from the peroxide to the surrounding π-groups[16,38]. Subsequently, the OOH• species may abstract hydrogen from TMB and a proton from imidazole–H, leading to the formation of H_2O and TMB•+.

It is noteworthy that the kinetic parameters, k_{cat} and k_{cat}/K_M, were estimated based on the assumption that all the histidine residues can participate in the catalysis. However, atomic force microscopy (AFM) images of the large-scale H15 nanostructures showed that the thickness ranged from around 1 nm to hundreds of nanometres (Supplementary Fig. 47). This observed thickness reflects the distances between the β-sheets, and the observed 1 nm is consistent with the height of a single β-sheet layer. Compared with the residues on facets (100) and (001), the residues exposed on facet (010) are much closer, pulling together H_2O_2 and TMB, and facilitating the transformation of the substrates. A theoretical simulation showed the inability of the aromatic TMB to diffuse into the catalyst because of steric hindrance (Supplementary Fig. 48). Therefore, k_{cat} and k_{cat}/K_M were underestimated and the actual values may be one or two orders of magnitude higher.

Trace impurities, such as iodide or transition metal ions, may exist in the self-assembled nanostructures and affect the catalysis by reacting with H_2O_2 to form ROS species (for example, OH•). We first used inductively coupled plasma mass spectrometry (ICP-MS) to identify the amount of trace impurities, and found all the impurities that may catalyse reactions were below 1 ppm, and most of them were below the detection limit (Supplementary Table 1). The residues, as potential ligands, were in large excess over the impurities. Thus, we added additional Zn^{2+}, Fe^{3+}, Cr^{3+}, V^{3+}, Cu^{2+}, Mn^{2+}, Co^{2+} and I^- in concentrations of up to 10 μM (~400 ppm) to the catalyst. No enhanced activity was observed (Supplementary Fig. 49). We also added ethylenediaminetetraacetic acid (EDTA; 10 μM), a strong metal chelator, which did not affect the activity in the oxidation of NADH and HVA (Supplementary Figs. 50a,b). However, TMB oxidation was inhibited, probably because EDTA can form a complex with TMB and inhibit the binding of H_2O_2 to TMB on the catalyst (Supplementary Fig. 50c,d and Discussion 2). This does not occur with NADH or HVA due to repulsion between these substrates and negatively charged EDTA. These results indicate that the presence of trace impurities do not contribute substantially to the activity of the catalyst.

Activity stimulation
The haemin-free catalysts catalysed redox reactions through cooperation with the organized histidine residues, which may dissociate and recover in heating and cooling treatments. The temperature of H15-catalysed reactions was cycled between 75 °C and 25 °C, and no loss of activity was observed after ten or more cycles (Fig. 6a and Supplementary Figs. 51 and 52). CD spectra (Supplementary Fig. 53) and XRD patterns (Supplementary Fig. 54) indicated that temperature cycling may result in reversible ordered and disordered arrangements of the residues, in essence, switchable active sites. In comparison, horseradish peroxidase (HRP; Fig. 5a and Supplementary Fig. 55) and artificial haemin-containing catalytic complexes (Supplementary Figs. 56 and 57) lost more than 90 and 80% activity, respectively, after ten temperature cycles. UV-Vis spectrophotometry showed the irreversible aggregation of haemin after the annealing of haemin-containing catalysts (Supplementary Fig. 58), which may be the cause of the loss of activity. We also investigated the response of H15 activity to acidification by cycling the pH between pH 7.0 and pH 1.0. No evident loss of activity was found after ten cycles (Fig. 6b and Supplementary Fig. 59), but HRP lost over 90% of its activity (Fig. 5b and Supplementary Fig. 63). Correspondingly, the molecular conformation of H15, the maximum absorbance wavelength, the morphology and the periodicity of the nanostructures (Supplementary Figs. 60–62) oscillated with the pH changes.
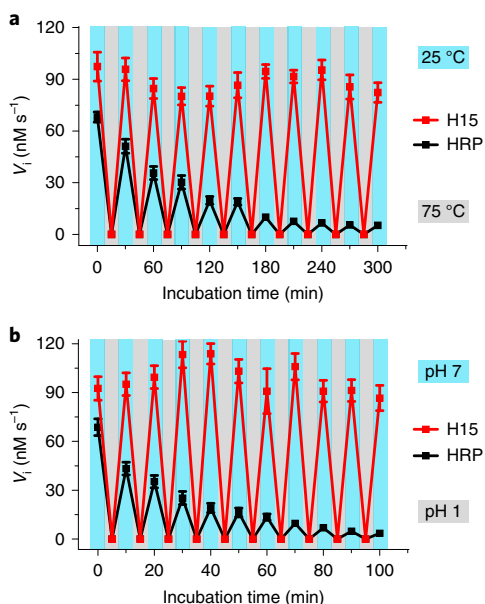
Fig. 6 | Externally triggered deactivation and activation of the H15 peptide and HRP. a,b, Effects of cycled heating and cooling treatments (**a**) and cycled acidification and neutralization treatments (**b**) on the catalytic oxidation of TMB by H_2O_2. The data in **a** and **b** are presented as the mean ± s.d., with the error bars representing the s.d. and N = 3.

Activity improvement

The apparent activity of the haem-free catalysts was several orders of magnitude lower than that of HRP (Supplementary Table 2), which has the most prominent activity of the haem-containing enzymes. The activity could be enhanced by increasing the catalytic surface area[8]. Ultrasonic treatment of H15-assembled catalysts increased the turnover frequency $k_{cat}^{H_2O_2}$ and k_{cat}^{TMB} by 2- and 3.7-fold, respectively, as a result of the decrease in particle size (Supplementary Fig. 64 and Discussion 3). As an alternative, the conjugation of a fibril-forming inert peptide ('Q11', QQKFQFQFEQQ)[39,40] with the oligohistidine led to the formation of nanoscale fibrils and increased the k_{cat} (for both substrates) by almost one order of magnitude compared with that of catalyst comprising only oligohistidine (Supplementary Fig. 65 and Discussion 4). Efforts to improve the activity of the haem-free catalysts through the aid of computational methods[41–43] to approach that of haem-containing enzymes is worthy of future study.

Outlook

We have described herein a strategy for designing cofactor-free oxidase-mimicking catalysts and a novel mechanism for catalysed electron-transfer reactions. These cofactor-free supramolecular catalysts provide a putative model for primitive enzymes, whose environmental-induced deactivation and activation could explain how these supramolecular peptide assemblies would survive under prebiotic conditions.

Online content

Any methods, additional references, Nature Research reporting summaries, source data, extended data, supplementary information, acknowledgements, peer review information; details of author contributions and competing interests; and statements of data and code availability are available at https://doi.org/10.1038/s41563-020-00856-6.

References

1. Bui, S. & Steiner, R. A. New insight into cofactor-free oxygenation from combined experimental and computational approaches. *Curr. Opin. Struct. Biol.* **41**, 109–118 (2016).
2. Hernandez-Ortega, A. et al. Catalytic mechanism of cofactor-free dioxygenases and how they circumvent spin-forbidden oxygenation of their substrates. *J. Am. Chem. Soc.* **137**, 7474–7487 (2015).
3. Wei, D. H. et al. Catalytic mechanisms for cofactor-free oxidase-catalyzed reactions: reaction pathways of uricase-catalyzed oxidation and hydration of uric acid. *ACS Catal.* **7**, 4623–4636 (2017).
4. Meeuwissen, J. & Reek, J. N. H. Supramolecular catalysis beyond enzyme mimics. *Nat. Chem.* **2**, 615–621 (2010).
5. Wiester, M. J., Ulmann, P. A. & Mirkin, C. A. Enzyme mimics based upon supramolecular coordination chemistry. *Angew. Chem. Int. Ed.* **50**, 114–137 (2011).
6. Wu, L. Z., Chen, B., Li, Z. J. & Tung, C. H. Enhancement of the efficiency of photocatalytic reduction of protons to hydrogen via molecular assembly. *Acc. Chem. Res.* **47**, 2177–2185 (2014).
7. Wang, T. T., Fan, X. T., Hou, C. X. & Liu, J. Q. Design of artificial enzymes by supramolecular strategies. *Curr. Opin. Struct. Biol.* **51**, 19–27 (2018).
8. Makam, P. et al. Non-proteinaceous hydrolase comprised of a phenylalanine metallo-supramolecular amyloid-like structure. *Nat. Catal.* **2**, 977–985 (2019).
9. Begley, T. P., Chatterjee, A., Hanes, J. W., Hazra, A. & Lick, S. E. E. Cofactor biosynthesis—still yielding fascinating new biological chemistry. *Curr. Opin. Chem. Biol.* **12**, 118–125 (2008).
10. Singh, N., Tena-Solsona, M., Miravet, J. F. & Escuder, B. Towards supramolecular catalysis with small self-assembled peptides. *Isr. J. Chem.* **55**, 711–723 (2015).
11. Ulijn, R. V. & Smith, A. M. Designing peptide based nanomaterials. *Chem. Soc. Rev.* **37**, 664–675 (2008).
12. Adler-Abramovich, L. & Gazit, E. The physical properties of supramolecular peptide assemblies: from building block association to technological applications. *Chem. Soc. Rev.* **43**, 6881–6893 (2014).
13. Carny, O. & Gazit, E. A model for the role of short self-assembled peptides in the very early stages of the origin of life. *FASEB J.* **19**, 1051–1055 (2005).
14. Romero, M. L. R., Rabin, A. & Tawfik, D. S. Functional proteins from short peptides: Dayhoff's hypothesis turns 50. *Angew. Chem. Int. Ed.* **55**, 15966–15971 (2016).
15. Greenwald, J., Kwiatkowski, W. & Riek, R. Peptide amyloids in the origin of life. *J. Mol. Biol.* **430**, 3735–3750 (2018).
16. Derat, E. & Shaik, S. The Poulos–Kraut mechanism of compound I formation in horseradish peroxidase: a QM/MM study. *J. Phys. Chem. B* **110**, 10526–10533 (2006).
17. Wan, L. L., Twitchett, M. B., Eltis, L. D., Mauk, A. G. & Smith, M. In vitro evolution of horse heart myoglobin to increase peroxidase activity. *Proc. Natl Acad. Sci. USA* **95**, 12825–12831 (1998).
18. Olson, J. S. et al. The role of the distal histidine in myoglobin and hemoglobin. *Nature* **336**, 265–266 (1988).
19. Liu, Q., Wang, H., Shi, X. H., Wang, Z. G. & Ding, B. Q. Self-assembled DNA/peptide-based nanoparticle exhibiting synergistic enzymatic activity. *ACS Nano* **11**, 7251–7258 (2017).
20. Marchetti, L. & Levine, M. Biomimetic catalysis. *ACS Catal.* **1**, 1090–1118 (2011).
21. Rufo, C. M. et al. Short peptides self-assemble to produce catalytic amyloids. *Nat. Chem.* **6**, 303–309 (2014).
22. Delort, E., Nguyen-Trung, N. Q., Darbre, T. & Reymond, J. L. Synthesis and activity of histidine-containing catalytic peptide dendrimers. *J. Org. Chem.* **71**, 4468–4480 (2006).
23. Deepak, R. N. V. K. & Sankararamakrishnan, R. N–H⋯N hydrogen bonds involving histidine imidazole nitrogen atoms: a new structural role for histidine residues in proteins. *Biochemistry* **55**, 3774–3783 (2016).
24. Song, Y. J., Qu, K. G., Zhao, C., Ren, J. S. & Qu, X. G. Graphene oxide: intrinsic peroxidase catalytic activity and its application to glucose detection. *Adv. Mater.* **22**, 2206–2210 (2010).
25. Gong, K. P., Du, F., Xia, Z. H., Durstock, M. & Dai, L. M. Nitrogen-doped carbon nanotube arrays with high electrocatalytic activity for oxygen reduction. *Science* **323**, 760–764 (2009).
26. Wang, X. C. et al. A metal-free polymeric photocatalyst for hydrogen production from water under visible light. *Nat. Mater.* **8**, 76–80 (2009).
27. Liu, X. & Dai, L. M. Carbon-based metal-free catalysts. *Nat. Rev. Mater.* **1**, 16064 (2016).
28. Ghosh, S. et al. Conducting polymer nanostructures for photocatalysis under visible light. *Nat. Mater.* **14**, 505–511 (2015).
29. Geng, G. W. et al. Shape-controlled metal-free catalysts: facet-sensitive catalytic activity induced by the arrangement pattern of noncovalent supramolecular chains. *ACS Nano* **11**, 4866–4876 (2017).
30. Liu, D., Wang, J., Bai, X. J., Zong, R. L. & Zhu, Y. F. Self-assembled PDINH supramolecular system for photocatalysis under visible light. *Adv. Mater.* **28**, 7284–7290 (2016).

31. Pellach, M. et al. Molecular engineering of self-assembling diphenylalanine analogues results in the formation of distinctive microstructures. *Chem. Mater.* **28**, 4341–4348 (2016).

32. Hu, K. et al. Tuning peptide self-assembly by an in-tether chiral center. *Sci. Adv.* **4**, eaar5907 (2018).

33. Miles, A. J. & Wallace, B. A. Circular dichroism spectroscopy of membrane proteins. *Chem. Soc. Rev.* **45**, 4859–4872 (2016).

34. Cerf, E. et al. Antiparallel β-sheet: a signature structure of the oligomeric amyloid β-peptide. *Biochem. J.* **421**, 415–423 (2009).

35. Goormaghtigh, E., Cabiaux, V. & Ruysschaert, J. M. Determination of soluble and membrane protein structure by Fourier transform infrared spectroscopy. I. Assignments and model compounds. *Subcell Biochem.* **23**, 329–362 (1994).

36. Marquez, L. A. & Dunford, H. B. Mechanism of the oxidation of 3,5,3',5'-tetramethylbenzidine by myeloperoxidase determined by transient- and steady-state kinetics. *Biochemistry* **36**, 9349–9355 (1997).

37. Josephy, P. D., Eling, T. & Mason, R. P. The horseradish peroxidase-catalyzed oxidation of 3,5,3',5'-tetramethylbenzidine. *J. Biol. Chem.* **257**, 3669–3675 (1982).

38. Campomanes, P., Rothlisberger, U., Alfonso-Prieto, M. & Rovira, C. The molecular mechanism of the catalase-like activity in horseradish peroxidase. *J. Am. Chem. Soc.* **137**, 11170–11178 (2015).

39. Rudra, J. S. et al. Self-assembled peptide nanofibers raising durable antibody responses against a malaria epitope. *Biomaterials* **33**, 6476–6484 (2012).

40. Rudra, J. S., Tian, Y. F., Jung, J. P. & Collier, J. H. A self-assembling peptide acting as an immune adjuvant. *Proc. Natl Acad. Sci. USA* **107**, 622–627 (2010).

41. Li, R. F. et al. Computational redesign of enzymes for regio- and enantioselective hydroamination. *Nat. Chem. Biol.* **14**, 664–670 (2018).

42. Li, F. et al. Design of self-assembly dipeptide hydrogels and machine learning via their chemical features. *Proc. Natl Acad. Sci. USA* **116**, 11259–11264 (2019).

43. Yu, F. T. et al. Protein design: toward functional metalloenzymes. *Chem. Rev.* **114**, 3495–3578 (2014).

Methods

Materials and reagents. All histidine peptides with different chain lengths were purchased from Shanghai ZiYu Biotech with a level of purity above 99%. Guanine-rich nucleic acid (purified by dual PAGE) was purchased from Invitrogen Life Technologies. Haemin, MES/MES sodium salt, H_2O_2, HRP, TMB, HVA, NADH, TBA and DMSO were purchased from Sigma-Aldrich. SOD was purchased from Macklin and BMPO was purchased from Dojindo. Water was deionized using a Milli-Q system.

Peptide synthesis usually involves trifluoroacetic acid (TFA) that is not easy to remove. ^{19}F NMR spectroscopic experiments were performed and residual TFA was indeed found. To remove TFA, the peptides were initially dissolved in deionized water at 10–100 mM concentration, and concentrated hydrochloric acid was added to yield final solutions with pH 1. Then, the samples were lyophilized overnight and redissolved in deionized water. The cycle of redissolving and lyophilization was repeated twice. No TFA signals were observed in the ^{19}F NMR spectra after this purification procedure (Supplementary Fig. 66).

Instruments. UV-Vis absorption spectra were recorded using a UV-2600 spectrometer equipped with a temperature-control accessory (Shimadzu). Fluorescent emission spectra were recorded with a DeltaFlex TCSPC system (HORIBA). Confocal imaging was carried out on a FV-1000 confocal microscope (Olympus; for Cy5, under a 635 nm channel) and analysed using the FV10-ASW software (Version 04.02.03.06, Olympus Corporation, 2013). AFM characterization was conducted on a Bruker MultiMode 8 microscope (Bruker Daltonics), and all samples were scanned in liquid ScanAsyst mode using ScanAsyst-in-Fluid tips. The AFM images were analysed using the NanoScope Analysis software (Build R2.103555, Bruker Corporation, 2013). SEM characterization was conducted using a SU8220 microscope (Hitachi). TEM morphological images were obtained at 80 kV in bright-field mode using an Hitachi 7700 microscope. SAED, elemental mapping and HRTEM were carried out on a JEM-2100F system equipped with a cooling stage and energy-dispersive X-ray spectrometer (JEOL). EPR measurements were conducted on an ELEXSYS-II E500 CW-EPR spectrometer (Bruker BioSpin). CD spectra were recorded with a J-1500 spectropolarimeter (Jasco). Powder XRD patterns were collected on a D/MAX-TTRIII(CBO) diffractometer equipped with a copper filter (Rigaku) under the following conditions: scan speed, $4° min^{-1}$, Cu Kα radiation, $λ = 1.54056$ Å. FTIR spectra were recorded on a Perkin Elmer Spectrum-One spectrometer equipped with a reflectance accessory at a resolution of $2 cm^{-1}$. Ten accumulations were acquired to improve the signal-to-noise ratio. NMR measurements were conducted on a Bruker Avance III HD 400 MHz spectrometer after dissolving the peptide samples in deuteroxide (D_2O). ^{19}F NMR spectra were recorded at a spectrometer frequency of 376.50 MHz. The pulse width was 18.0 μs, the relaxation time was 1.0 s and the acquisition time was 0.734 s. In total, 16 scans were recorded for each analysis. Qualitative and quantitative elemental analyses were conducted using an Agilent 8800 Triple Quadrupole ICP-MS to detect all metallic elements at a 1 ppb detection limit and non-metallic elements at a 1 ppt detection limit.

Sample preparation for characterization. (1) For SEM imaging, the self-assembled oligohistidine peptide solution was dropped onto a glow-discharged silicon wafer and left for 1 h, followed by wicking away of the unbound sample and solution evaporation. Before characterization, a thin layer of platinum particles was sputtered onto the surface. (2) For TEM imaging, 10 μl peptide solution was deposited onto a glow-discharged carbon-coated grid for 20 min, followed by removal of excess solution with filter paper and solution evaporation. (3) For AFM imaging, 10 μl self-assembled peptide sample was left to adsorb on a glow-discharged silicon wafer for 1 h. Then, 200 μl MES buffer (pH 7.0) was added to the liquid cell. (4) For the XRD measurements, the self-assembled peptide solution was desalinated through Amicon Ultra centrifugal filters (Ultracel-3 K, Merck Millipore) to remove MES sodium salt in the buffer, then lyophilized using a freeze dryer. (5) For the FTIR measurements, the self-assembled peptide sample was desalinated and lyophilized as described for the XRD measurements. Then, the lyophilized sample was redissolved in deuteroxide to allow hydrogen/deuterium exchange and then lyophilized again.

Activity assay. The as-purified peptide samples were dissolved in deionized water to make 10 mM stock solutions. Then, the peptides were added to 50 mM MES buffer (pH 7.0) at the required concentrations, followed by incubation at room temperature for 6 h. With TMB and H_2O_2 as the substrates, the reactions were performed at pH 7.0. With NADH and H_2O_2 as the substrates, the pH of the solution was adjusted to 6.0 using HCl. With HVA and H_2O_2 as the substrates, the pH value was adjusted to 8.0 using NaOH. Time-dependent absorbance and fluorescence changes were recorded, and the data were used to calculate the initial catalytic velocity (V_i). For the pH and thermal treatment of the catalytic systems, HRP was treated at 1, 10 or 100 μM, and diluted to 1 nM for the activity assay; haemin (contained in the artificial complexes) was treated at 10 or 100 μM, and diluted to 1 μM for the activity assay.

Simulation. Both quantum chemical calculations and molecular docking were conducted to gain a better understanding of the active site by exploring the structures and interactions of the oligohistidine peptide-assembled nanostructures, H_2O_2 and TMB. The crystal structures of H15 and H2 together with the co-adsorption of TMB and H_2O_2 were studied by first-principles calculations. All the calculations were performed using the Vienna ab initio simulation package and the plane-wave pseudopotential method[44,45]. Electronic exchange and correlation effects were described by the Perdew–Burke–Ernzerhof functional[46] with the generalized gradient approximation, and the core electrons were described by the full-potential projector augmented wave method[47,48]. An energy cut-off of 400 eV for the plane-wave expansion was used and the force on the relaxed atoms was less than $0.03 eV$ $Å^{-1}$. Spin polarization was taken into account in all calculations. The Brillouin zone was sampled using the k-point grid generated within the Monkhorst–Pack scheme: ($1 × 10 × 4$) for H15, ($5 × 4 × 10$) for H2 and ($1 × 1 × 1$) for the co-adsorption of TMB and H_2O_2.

The peptide conformations from the first-principles calculations were used for molecular docking analysis. Molecular H_2O_2 and TMB as ligands were optimized using the Gaussian 09 program at the B3LYP/6-31G* level of theory[49–51]. All the molecular docking simulations were carried out with Lamarckian genetic algorithm using Auto-Dock 4.2.6[52]. A grid box big enough to cover the entire surface of the peptide was implemented. The conformations with lowest binding energy were selected for the detailed analysis.

Statistical analysis. The methods used for statistical analysis are specified in the results sections or figure captions for the quantitative data. All values are reported as mean ± s.d. with the indicated sample size. All relevant statistical tests were two-sided. Statistical analyses were performed using the GraphPad Prism 5 software.

Data availability

The data that support the findings of this study are available within the paper and its Supplementary Information files. Additional data and files are available from the corresponding authors upon reasonable request.

References

44. Kresse, G. & Furthmuller, J. Efficient iterative schemes for ab initio total-energy calculations using a plane-wave basis set. *Phys. Rev. B* **54**, 11169–11186 (1996).
45. Kresse, G. & Hafner, J. Ab initio molecular dynamics for liquid metals. *J. Non-Cryst. Solids* **47**, 558–561 (1993).
46. Perdew, J. P., Burke, K. & Ernzerhof, M. Generalized gradient approximation made simple. *Phys. Rev. Lett.* **77**, 3865–3868 (1996).
47. Blochl, P. E. Projector augmented-wave method. *Phys. Rev. B* **50**, 17953–17979 (1994).
48. Kresse, G. & Joubert, D. From ultrasoft pseudopotentials to the projector augmented-wave method. *Phys. Rev. B* **59**, 1758–1775 (1999).
49. Frisch, M. J. et al. Gaussian 09 (Gaussian, Inc., 2013).
50. Stephens, P. J., Devlin, F. J., Chabalowski, C. F. & Frisch, M. J. Ab initio calculation of vibrational absorption and circular dichroism spectra using density functional force fields. *J. Phys. Chem.* **98**, 11623–11627 (1994).
51. Hariharan, P. C. & Pople, J. A. The influence of polarization functions on molecular orbital hydrogenation energies. *Theor. Chem. Acc.* **28**, 213–222 (1973).
52. Morris, G. M. et al. Autodock4 and Autodocktools4: automated docking with selective receptor flexibility. *J. Comput. Chem.* **30**, 2785–2791 (2009).

Author contributions

Z.G.W. and B.D. conceived and designed the experiments. Q.L., Y.Z., Y.S. and L.D. performed the experiments. Z.G.W., B.D., Q.L. and H.W. collected and analysed the data. D.L. and C.W. provided suggestions and technical support on the project. H.W., K.W. and X.S. performed the theoretical simulations. Z.G.W. and B.D. supervised the project. Z.G.W., B.D., H.W. and Q.L. wrote the manuscript. All authors discussed the results and commented on the manuscript.

Competing interests

The authors declare no competing interests

Additional information

Supplementary information is available for this paper at https://doi.org/10.1038/s41563-020-00856-6.

Correspondence and requests for materials should be addressed to Z.-G.W., H.W. or B.D.

Reprints and permissions information is available at www.nature.com/reprints.